

Spectrum on demand light source (SOLS) for advanced photovoltaic characterization

Cite as: Rev. Sci. Instrum. 94, 103907 (2023); doi: 10.1063/5.0156236

Submitted: 27 April 2023 • Accepted: 3 October 2023 •

Published Online: 20 October 2023



View Online



Export Citation



CrossMark

Miquel Casademont-Viñas,¹ Martí Gibert-Roca,¹ Mariano Campoy-Quiles,¹ and Alejandro R. Goñi^{1,2,a)}

AFFILIATIONS

¹ Materials Science Institute of Barcelona, ICMAB-CSIC, Campus of the UAB, 08193 Bellaterra, Barcelona, Spain

² ICREA, Passeig Lluís Companys 23, 08010 Barcelona, Spain

^{a)}Author to whom correspondence should be addressed: goni@icmab.es

ABSTRACT

We report a multi-purpose spectrum-on-demand light source (SOLS), conceived primarily but not exclusively for the multiple and advanced characterization of photovoltaic (PV) materials and devices. The apparatus is a spectral shaper illumination device, providing a tunable and spectrally shaped light beam produced by modulating the intensity and/or wavelength range of a primary light source. SOLS stands out from the state of the art because it produces almost any spectrum on demand and delivers two types of output: a spectrally shaped and spatially homogeneous beam over its cross section for areal illumination or a spatially and spectrally split beam into its wavelength components, a unique capability suited to characterize lateral-tandem (Rainbow) solar cells. The tuneability from broadband to narrowband illumination enables two characterization devices into one, namely, a solar simulator for the determination of the power conversion efficiency and an external quantum efficiency measuring system. We expect the SOLS setup to accelerate material screening, enabling the discovery and optimization of novel multi-component materials and devices, in particular for emergent PV technologies like organic, metal halide perovskites, or multi-junction geometries, as well as novel PV applications such as indoors, building integrated, or agrivoltaics, among others.

Published under an exclusive license by AIP Publishing. <https://doi.org/10.1063/5.0156236>

I. INTRODUCTION

The photovoltaic (PV) effect is an effective mechanism for converting the solar energy reaching Earth's surface ($\sim 1000 \times$ the total energy consumption worldwide) into electricity.^{1,2} The current PV market is dominated by silicon based solar cells, primarily due to their cost-effectiveness and mature manufacturing processes.³ However, emerging PV technologies based on alternative materials, such as organic molecules, polymers, semitransparent oxides, kesterites, quantum dots, or hybrid halide perovskites, are becoming increasingly relevant in the field of PV research.^{4,5} These technologies have desirable traits like lower potential cost, scalable solution-processing manufacturing, short energy payback times, semi-transparency, flexibility, color tuning, and being lightweight, which render them promising candidates for commercialization. Furthermore, many of these emerging technologies are inherently sustainable, relying on the use of abundant and (mostly) non-toxic raw materials.⁶ One important feature of the materials employed in these emerging

technologies is that their optical and electronic properties can be tuned through synthesis.^{7–10} This, on the one hand, is routinely used in order to improve device power conversion efficiency and stability, for instance, in multi-cation perovskite solar cells¹¹ or ternary organic photovoltaics.¹² On the other side, the aforementioned tuneability opens the possibility of making photovoltaic technologies adapted to different applications, such as indoor, semitransparent windows, agrivoltaics, etc. This tunability has also promoted research in multi-junction geometries,^{13,14} in which materials of different bandgaps harvest sunlight more efficiently in order to increase power conversion efficiency.

The development and optimization of materials for emergent photovoltaic technologies tailored for different conditions and environments are increasingly calling for novel light sources capable of adapting the irradiance conditions to the targeted application. Examples include modules placed on vertical walls (e.g., for building integrated PV¹⁵) at different altitudes (thus different UV amounts¹⁶), different air masses and turbidities,¹⁷ underwater

photovoltaics,¹⁸ or for indoor applications.^{19,20} Recently, multi-junction solar cells based on the spectral splitting concept have attracted renewed attention.^{21,22} In this case, an optical element separates the sunlight into a number of beams exhibiting different spectra in order to match the spectral range with the bandgap of each sub-cell. In order to optimize this geometry, each sub-cell should be investigated as a function of a fraction of the sun spectrum. This would require sources capable of producing a tunable low bandpass, a high bandpass, and a narrow bandpass. In fact, while very promising results have been obtained for different applications, we believe the field would greatly benefit from novel characterization tools that could help adapt studies to specific geometries and applications (*vide infra*).

A reference figure of merit in solar cells is the power conversion efficiency (PCE) under 1 sun illumination (the standard terrestrial AM1.5 G broadband spectrum). To determine the PCE, the current–voltage (J–V) dependence of the solar cell is measured while being illuminated with a solar simulator, a source that emulates the solar irradiance spectrum by coupling spectral filters with a broadband lamp (e.g., halogen, Xenon arc, etc.).^{5,23} Another essential specification is the external quantum efficiency (EQE), which provides information on the photon-to-electron conversion effectiveness. The EQE is obtained by short circuiting the solar cell and measuring the output current while it is being illuminated with a narrowband monochromatic light source. Such a narrowband light source is typically attained by spectrally filtering a broadband source with a monochromator. By sweeping the peak wavelength of this monochromatic light throughout a selected wavelength range, the electrical response of the cell is obtained at each particular wavelength, yielding the EQE spectrum.⁵ Besides PCE and EQE measurements, more advanced measurements have also been proposed for the in-depth investigation of solar cells. For instance, the dependence of the photocurrent and open circuit voltage on illumination intensity has been used to investigate different recombination mechanisms in organic^{24–26} and hybrid²⁷ based photovoltaics. Experimentally, this is achieved by attenuating the light from a solar simulator between two and four orders of magnitude using neutral density filters.

Currently, these measurements rely on the use of different filters and/or different light sources and/or different setups. Importantly, a recent attractive method to have a light source whose light spectrum can be modified in shape and intensity is by using an array of individually addressable light emitting diodes (LEDs), which are particularly useful to produce different broadband spectra (e.g., AM0 and AM1.5G) as well as different narrowband spectra.^{23,28,29} Having a single piece of equipment for testing many conditions is indeed very advantageous. However, LED illumination has several intrinsic limitations, such as poor spectral resolution (typical systems have <20 LEDs to cover a spectral range of more than 900 nm; thus, the LEDs used for these devices have FWHMs of several tens of nanometers and, therefore, EQE measurements or spectral splitting measurements have poor resolution). Another problem is the non-linear response of LEDs to current, which strongly limits the dynamic range of the illumination source. The latter implies that LED based solar simulators may not be well fitted for experiments requiring strongly tuning the light intensity (e.g., the aforementioned recombination studies) or to reproduce indoor illumination conditions unless a combination of (non-automatic) filters is used.

Besides LED arrays, other pieces of equipment have been introduced for modifying the incoming spectrum. For instance, diffraction-based filters (i.e., using diffraction gratings) have been introduced for spectrum customization.³⁰ Unfortunately, these suffer from a limited wavelength range and the loss of a significant fraction of light intensity due to diffraction in higher orders.

In terms of beam characteristics, all the discussed characterizations require the beam to be homogeneous in terms of intensity and spectrum as well as stable over time. Therefore, the different light sources (broadband lamps, LED arrays, monochromators, and grating based filters) are set up to do this. There is one notable exception for this requirement: the mentioned multi-junction solar cells based on the spectrally split (Rainbow) concept.²¹ Here, a spectrally split beam is required so each sub-cell can be illuminated with the appropriate fraction of the sun spectrum. Notably, what defines the appropriate fraction is the bandgap of the materials used in each sub-cell and, therefore, a highly tunable setup is required to investigate and optimize this geometry.

In this work, we present a Spectrum-On-demand Light Source (SOLS) capable of providing a tunable light spectrum that can be spectrally shaped in intensity and/or wavelength range with respect to a primary light source. The distinctive features that differentiate the SOLS light source from the current state of the art are as follows:

1. It offers two types of spectrally shaped output: a *spatially homogeneous* beam over its cross section with the demanded spectral shape, used for homogeneous areal illumination; and a *spatially and spectrally split* beam divided into different wavelength components, a unique capability for illuminating lateral-tandem (Rainbow) solar cells.
2. It provides a *high light throughput* and a *large spectral window* (at least from 380 to 1100 nm) by implementing refractive/reflection optic elements, as compared to setups based on diffraction gratings or the like, for which a substantial part of the incoming light is wasted in feeding higher diffraction orders that also strongly limit the spectral range.
3. It can output a *highly tunable broad-band* spectrum shaped to suit a large range of applications, e.g., AM1.5, AM0, indoors, building integrated PV, agrovoltaics, a tunable low/high pass filter for spectral splitting PV, stability measurements, etc. At the same time, it can *automatically* output *narrow-band* spectra with a broad tunability of the central wavelength and FWHM, suitable for EQE measurements, among others.
4. SOLS has a *large intensity dynamic linear range* (about two orders of magnitude) that is realizable without the need for optical density filters, which could compromise the broadband spectral filtering uniformity. The intrinsic linearity in the intensity variation and its wide dynamic range lead to a much simpler and less time-consuming procedure to spectrally shape the output spectrum as compared to LED solar simulators.
5. SOLS exhibits *excellent temporal stability* in terms of intensity (e.g., <2%, type A solar simulator) and fairly good spatial homogeneity in terms of intensity (e.g., <5%, type B) and spectral shape over the output illuminated area.

In short, SOLS offers *great versatility* encompassing two different operation modes and all the mentioned features, making

it a powerful tool for the characterization of different PV properties like PCE, EQE, efficiency under specific illumination conditions, tandem optimization, light intensity scans, etc., while simultaneously adapting the output spectrum to match the illumination requirements of a particular application.

II. SETUP

The underlying concept for the proposed setup involves three main blocks. First, white light coming from a broadband lamp is dispersed into its constitutive wavelengths. The light beam after this stage consists of fringes of the different colors spatially separated (as if it were a rainbow). At this stage, a second block consisting of a shadow mask system is placed to block parts of the beam to reduce partially or totally the intensity of each color fringe. Alternatively, a third block can be added to the setup to mix the filtered beam to obtain a spatially homogeneous beam with the modified spectrum.

The inner workings of the setup as well as an illustrative schematic of the optical elements are shown in Fig. 1. The description follows the order given by the numbering of the elements, which corresponds to the direction of light propagation:

- (1) An incoming collimated light beam passes through a dispersive double Amici prism that separates the beam into its composing wavelengths only along one direction in a horizontal plane (X-Y plane).^{31,32} In our implementation, the light source is a Xenon arc lamp, but it can be any (broadband) light source. The main advantage of the double Amici prism compared to other types of dispersive prisms is that a certain wavelength of the incoming beam (550 nm for our

prism) remains in the optical axis, facilitating the geometric design of the optical setup. The wavelengths around the central wavelength will exit the Amici prism with a concrete deviation angle according to the refractive index dispersion of the different materials (see supplementary material, Sec. S1, Fig. S1). For a better light separation, the incoming beam should be as collimated as possible, since any degree of divergence or convergence of the input light will result in different incoming light angles and therefore different exit angles for the same wavelength, resulting in a poorer color separation. The latter is also affected by the width of the incoming light beam since a wider collimated input light will result in a wider spatial distribution of the same wavelength that leaves the prism with the same angle.

- (2) The spectrally split beam is reflected by a silver mirror with customized curvature (see supplementary material, Sec. S1, Fig. S2) that corrects the divergence applied by the prism to unify the spectrum (different colors) again into an illumination spot, re-concentrating the light in the X-Y plane. This mirror was calculated, designed, and fabricated within our group, as it is not commercially available. A 3D printed structure provides the calculated curvature of an evaporated silver-coated 0.5 mm thick rectangular piece of polyethylene terephthalate glycol-modified (PETG). In addition, the distance that the spectrally split beam is forced to travel needs to be adjusted to guarantee a correct spatial wavelength separation to attain the desired wavelength resolution. In our implementation, the distance between the prism and the curved mirror is about 30 cm.
- (3) A spatially filtering element is placed in the beam path in a position where the beam color components are still separated. This filtering element is one of the key components that enables spectral shaping in a simple and versatile manner. The filtering element blocks light at certain spatial positions on the plane perpendicular to the beam propagation, defined by two orthogonal directions: one in which light becomes spectrally separated (the intersection with the X-Y plane); and the other one, in the Z direction, corresponding to the actual height of the light beam, which determines the intensity of each color, as depicted in Fig. 1 (3.1). The simplest way to block parts of the beam is by using any kind of light blocking element, i.e., a “shadow mask,” in this position. For demonstration, we have implemented the use of 3D printed “cards” (3.1 in Fig. 1 and Fig. S3 in the supplementary material), such that by insertion of a card with a given slit-height vs wavelength profile, a predefined spectrum is obtained (see also Fig. 2). The mask encodes the intensity-versus-wavelength information in the form of slit-height as a function of lateral position, which can be calculated assuming a linear combination of the spectrum resulting from each separated slit. This process, called slit mask calibration, is explained in detail in the supplementary material, Sec. S2. The first filter element is static and could be used for PCE measurements under many different illumination conditions, such as AM1.5, indoors, or underwater. For more advanced experiments, we have introduced a partial automatization of the filtering process, consisting of adding a second, motorized filtering stage. We

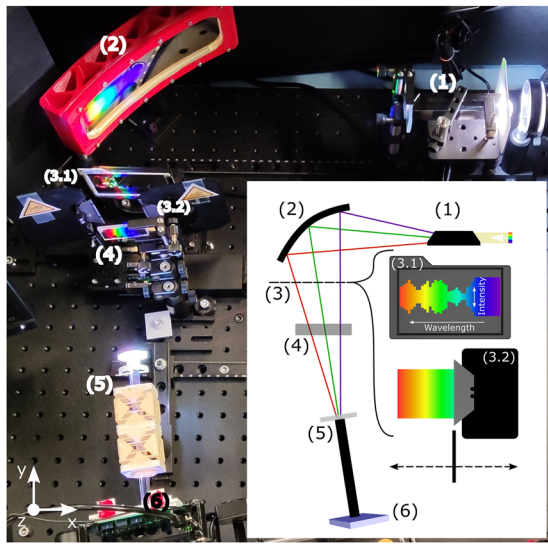


FIG. 1. SOLS setup and schematic drawing (inset), wherein the main parts are labeled as (1) double Amici prism; (2) custom mirror to concentrate light in the XY plane; (3) plane to physically block light by (3.1) custom masks and/or (3.2) moving guillotines; (4) cylindrical lens to concentrate light in the vertical (Z) direction; (5) light pipe homogenizer; and (6) light output and cell holder.

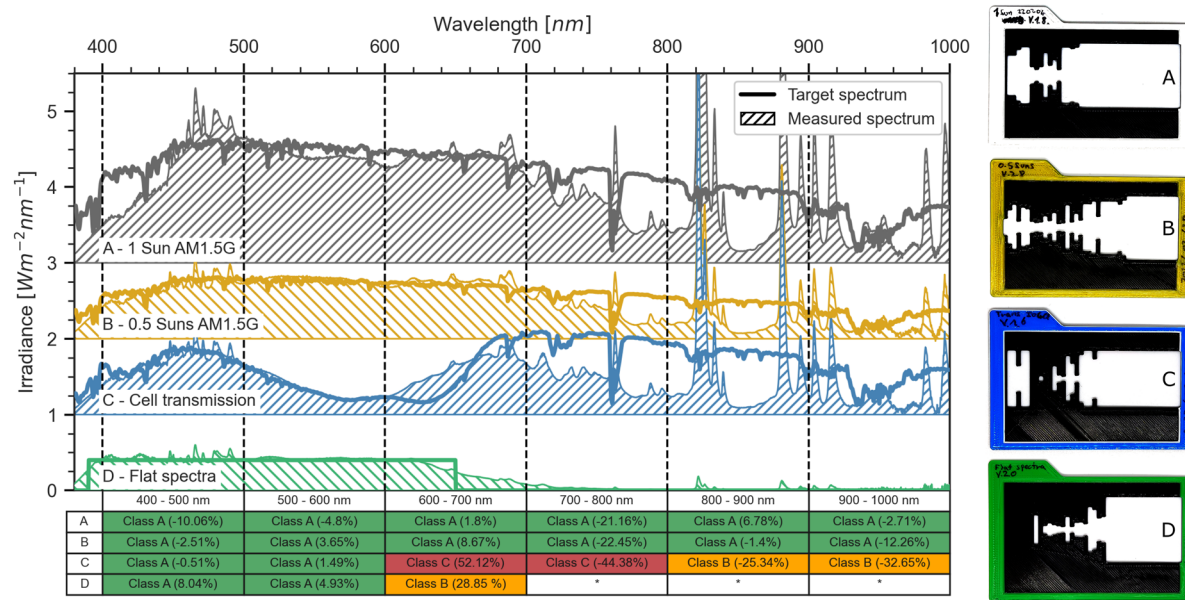


FIG. 2. Example of four different target spectra (dashed) and their corresponding SOLS output spectra (solid) made with the slits calibration system. The four spectra are spectrally evaluated (bottom panel) following the ASTM E927-10 standards. On the right panel, we show the 3D printed masks used for each of the measured spectra. (*) Corresponds to data that cannot be evaluated with the standards since the target spectra irradiance is 0; therefore, the percentage difference cannot be calculated.

have implemented in the setup (3.2 in Fig. 1 and Fig. S4 in the supplementary material) a system of two guillotines translated automatically by motors. Each guillotine cuts the spectrum completely above or below a given wavelength, producing the function of a tunable high pass, low pass, or band pass filter. As described below, these filtering elements can be used for spectral-splitting solar cell characterization and optimization. Because those two elements do not need to be on the same plane, one can have the effect of a filter (3.2) on a particular spectrum card (3.1), increasing even more flexibility in the design of the output spectrum.

- (4) A cylindrical lens concentrates the beam along the vertical (Z) direction (intensity) to provide a tight focus on the next optical element. The focal length matches the focus of the mirror in the horizontal direction (X-Y) in order to be on focus in both directions to ensure minimal light losses.
- (5) In the path and at the focal plane where light is being concentrated [where element (5) is placed in Fig. 1], the equipment delivers a focused but spectrally split beam. This could be used for the characterization of a Rainbow solar cell multi-junction device²¹ by placing the solar cell at the correct distance before or beyond that focal plane. Alternatively, a homogenizing device consisting of a diffusing element in front of a homogenizing light pipe can be placed at the focal point (5). In this way, the diffusing element introduces significant randomness in the direction of the incoming light, as shown in Fig. S5 of the supplementary material, such that together with the homogenizing light pipe, the output beam produces a homogeneous area of illumination, both

spectrally and intensity wise. In our current implementation, the resulting illuminated area (6) is about 55 mm² (a 4 mm inner radius hexagon).

- (6) Last but not least, the light output (6) needs to be characterized in terms of spectral irradiance (i.e., quantification of the power density per wavelength) in order to ascertain that the output spectrum matches the target spectrum as much as possible. The procedure followed for the characterization and calibration of the output spectrum is described in the supplementary material, Sec. S3.

III. APPLICATION EXAMPLES IN PHOTOVOLTAIC CHARACTERIZATION

A. Custom spectrum light source

With the presented tunable light source, it is possible to produce almost any desired spectral output by spectrally cropping that of a primary light source, i.e., by subtracting light from the input spectrum at specific wavelengths. This can be done using the mask card element (3.1) in Fig. 1, the specific shape of which can be calculated by following the calibration procedure described in Sec. S3 of the supplementary material. The great spectrum tunability can be seen in Fig. 2, where we show four examples of different target spectra (solid lines) and their corresponding SOLS measured output spectra (shaded curves). These spectra are complemented by the ASTM E927-19 classification (at the bottom), which compares the target spectrum with the real output spectrum in the relevant wavelength ranges.

The first targeted spectrum is the AM1.5G, where the SOLS output spectrum results in a *Class A* qualification between 400

and 1000 nm, making it suitable for standard PV characterization under 1 sun illumination. To confirm the suitability of the SOLS output spectrum, we measured 3 different OPV solar cells with both the SOLS and a calibrated commercial AAA solar simulator as light sources, resulting in less than a 5% difference for each of the measurements (Fig. S9 of the supplementary material).

The next curve corresponds to the 0.5 Sun AM1.5G spectrum exhibiting a *Class A* qualification as well, between 400 and 1000 nm, and proving the setup's ability to perform light intensity dependent PV characterization. With the current SOLS embodiment, the spectral intensity can be varied by ca. two orders of magnitude. By scaling the slit height-profile of a mask card while maintaining the same spectral shape, the integrated spectral intensity can be substantially varied from 0.01 to $1.5 \times$ AM1.5 (see the supplementary material, Sec. S5). Therefore, the dynamic spectral range of the SOLS is much wider than that of currently available spectral shaping alternatives, like the LED based solar simulator, enabling the study of light intensity dependent phenomena in greater detail. For example, this feature would be really useful to study the nature of recombination processes taking place in the photoactive layer, which requires measuring multiple J-V curves with a range of light intensities while maintaining the same input spectrum shape.^{25,26,33}

The SOLS is not limited to uniform intensity variations. By varying the relative intensity of each wavelength component, we can emulate the transmission spectrum of semitransparent solar cells, which can be a really interesting feature in the thickness and blend composition optimization of tandem PV. As an example, in Fig. 2(c), we emulate the transmission spectrum of a thin PBDBT-2F:IO-4Cl organic solar cell, which would act as the tandem top cell with a band gap located around 700 nm. With this "filtered" transmission spectrum, one can study the performance of multiple bottom cells before having to manufacture the actual tandem device.

Besides simulating the pure or "filtered" solar spectrum, the SOLS is capable of producing entirely custom shaped spectra, like the one shown in Fig. 2(d) (green curve), which targets a top-hat flat spectrum with an intensity of $0.4 \text{ W m}^{-2} \text{ nm}^{-1}$, between 400 and 650 nm, and $0 \text{ W m}^{-2} \text{ nm}^{-1}$ in every other wavelength. As we can see, the real output spectrum is also *Class A* within the relevant wavelength range, fitting the target spectrum quite well. This custom output spectrum capability expands the possible applications of the SOLS beyond PV characterization. As an example, these custom spectra could be used for calibration purposes that require a "white" spectrum, i.e., a wavelength-independent intensity. Other examples, such as a spectrum resembling the Barcelona skyline or a number of examples of spectra for use in indoor PV, can be found in the supplementary material, Sec. S6, Figs. S12 and S13.

The current SOLS embodiment exhibits poorer wavelength separation at longer wavelengths. This can be attributed to the use of dispersive prisms, which tend to have a more pronounced dispersion at shorter wavelengths.³² This can be seen in Fig. 2(c), where the SOLS output departs from the target spectrum around the NIR. However, as we discuss further below, we have proposed alternative configurations that effectively improve the SOLS spectral resolution.

B. Spectral splitting photovoltaics

Multi-junction solar cells can have several geometries. The most common one is known as tandem, in which sub-cells are

vertically stacked one on top of the other [see Fig. S15(a)]. In this geometry, the need for current matching between the multiple cells connected in series makes the optimization of the whole stack challenging. For example, the thickness of each sub-cell is crucial for the generated photo-current as well as light distribution inside the cell. This could be mitigated with SOLS by using the idea of the previous section [Fig. 2(d)], where the output light of the SOLS resembles light that would be transmitted through the top sub-cell(s).

There is another type of multi-junction geometry called spectral splitting, in which an optical element divides the spectrum into different complementary fractions and redirects each one to the most suitable sub-cell. One of the most studied spectral splitting geometries is shown in Fig. S15(b), where the optical element is a dichroic mirror and sub-cells are placed perpendicular to each other. Figure S15(c) shows a thus far less explored multi-junction spectral splitting geometry, where cells are placed next to each other. In this case, the light is redistributed in the sub-cell plane by a dispersive optical element, such as a Fresnel lens. Notice that the evaluation and optimization of spectral splitting geometries, in general, requires spectrally splitting the incoming light beam into beams with complementary spectra in a tunable way. To the best of our knowledge, there is no commercially available product that can produce such a *spectrally and spatially split* beam.

There is, therefore, a need for equipment able to characterize multi-junction solar cells comprising spectral splitting geometries. On the one hand, the desired equipment must be able to provide the corresponding spectrum that one sub-cell would receive in spectral splitting geometry, spanning a certain wavelength range.²¹ The SOLS apparatus is able to produce this kind of spectra thanks to the moving guillotines system (mask element 3.2). This system consists of two motorized guillotines that mask either the shorter wavelength (blue) part of the spectrum, acting as a high wavelength pass filter, or the longer wavelength (red) part of the spectrum, acting as a low wavelength pass filter (see Fig. S4). The motorization allows for tuning the low/high wavelength pass filter in a continuous way. Notice that the combination of both filters results in a band pass filter, which is also necessary for characterizing spectral splitting multi-junction geometries with at least three sub-cells.

We next give an example of a measurement made with SOLS in spectral splitting mode (Fig. 4 and Fig. S16 of the supplementary material). First, we will describe how the measurements were made. In this case, the characterization is carried out for a lateral tandem (Rainbow) with only two sub-cells, namely "blue" and "red" sub-cells with higher and lower bandgaps, respectively. Under AM1.5G illumination and in spectral splitting geometry, the red sub-cell receives the lower energy part of the solar spectrum from $\sim 1100 \text{ nm}$ up to the dividing wavelength λ_d , whereas the blue sub-cell receives the complementary part, i.e., between λ_d and 390 nm . The aim of the experiment is to determine the optimum λ_d . The measurements were performed with the card mask of the 1 Sun AM1.5G spectrum [Fig. 2(a)] and then moving the motorized guillotines (3.2) and recording the J-V response of the cell at each guillotine position with a λ_d step of 5 nm. The measurement procedure is as follows: each sub-cell is subsequently placed at the end of the homogenizing light pipe [point (6) of Fig. 1] for homogeneous illumination. Then, the response of the red sub-cell is determined for a so-called "red sweep," for which the starting position of the guillotine is at $\sim 390 \text{ nm}$, where the red sub-cell is illuminated with the full

spectrum, and then moves to the red up to ~ 810 nm. On the contrary, for the blue sub-cell, illumination proceeds as a “blue sweep,” in which the opposite guillotine starts at ~ 810 nm, again allowing full spectrum illumination, but moves to the blue toward 390 nm.

The mentioned λ_d of 810 nm is, for the time being, the practical upper bound limit of the setup due to the current low color separation in the red and IR regions and corresponds to a spectrum with almost no light for a red sweep and a full spectrum for a blue sweep. The actual λ_d low-wavelength limit of the setup is 390 nm, which outputs a null spectrum for the blue sweep and the full spectrum for the red sweep.

An example of the spectra resulting from a red sweep as a function of the moving guillotine is shown in Fig. 3. This red sweep dataset is used to calibrate the λ_d as a function of the red and blue motor positions, as explained in the supplementary material, Sec. S9. In this way, for each position of the guillotine corresponding to a λ_d , the red sub-cell receives only the red part of the full spectrum and the blue sub-cell receives the complementary blue part of the spectrum, as would be the case in a monolithically integrated lateral multi-junction (Rainbow) cell.²¹

In Fig. 4, we show the PCE results of a 2-junction Rainbow characterization with SOLS as a function of the λ_d corresponding to the measurement described before. The blue sub-cell PCE contribution (in blue) is measured with SOLS using the AM1.5 G mask shown in Fig. 2(a) and applying a blue sweep with the guillotines system with a λ_d spacing of 5 nm. Comparably, the red sub-cell (in red) was characterized with a red sweep for the same set of λ_d values. The sum of both sub-cell PCEs (in green) is the efficiency that a Rainbow device, composed of the corresponding sub-cells, would achieve at each λ_d . In this case, the Rainbow characterization made with SOLS reveals that the best Rainbow geometry is achieved with a dividing wavelength of 700 nm (vertical dotted green line), improving up to 46.6% the efficiency of the best single-junction cell, which is the red cell. The dividing wavelength dependence of all other parameters is shown in Fig. S16 in the supplementary material.

To the best of our knowledge, SOLS is the first and only device that can make this characterization, therefore making it relevant

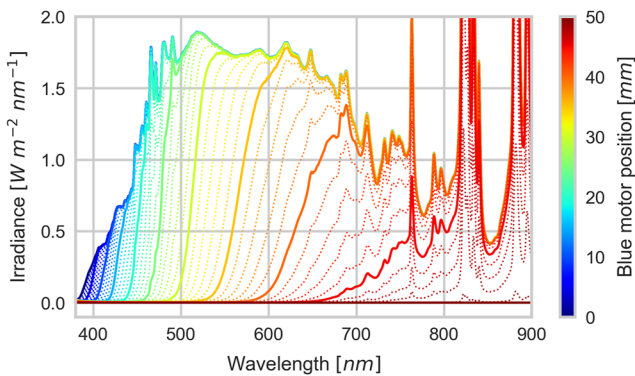


FIG. 3. SOLS output spectra as a function of the guillotine position corresponding to a red sweep. The guillotine distance between each spectrum is 1 mm; solid lines indicate positions that are multiples of 5 mm.

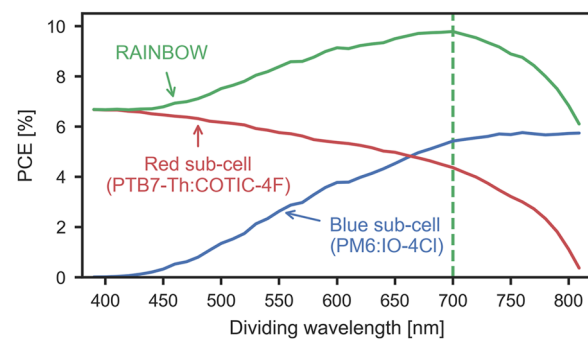


FIG. 4. Example of a Rainbow power conversion efficiency (PCE) characterization made with SOLS acquired with both filtering elements (guillotines and mask cards) in use. The PCE contribution of each sub-cell to the Rainbow PCE results from the J-V curve measurement in a red or blue sweep mode with a λ_d spacing of 5 nm between 390 and 810 nm. The green vertical dashed line marks the dividing wavelength that maximizes the PCE of the Rainbow device, which corresponds to a λ_d of 700 nm. In the present case, the increase in PCE over the best single junction cell is 46.6%.

for the future development of multi-junction lateral-tandem photovoltaic devices. Furthermore, details on the geometry of Rainbow solar cells can be found in our previous work.²¹ Notice that the dependence on λ_d of the performance of single-junction cells can be characterized with this methodology, enabling the determination of the maximum Rainbow efficiency and optimal λ_d for any pair of sub-cells. This is relevant from a high throughput point of view, meaning that there is no need to manufacture the actual monolithic Rainbow solar cell to know its optimal multi-junction efficiency.

On the other hand, in order to make the final verification of the monolithic devices, ideal equipment for the characterization of lateral multi-junction Rainbow solar cells must also provide a measurement mode in which the beam is split both spectrally and spatially, such that each sub-cell receives simultaneously the spectrum between previously defined dividing wavelengths. In the SOLS setup, this could be done by replacing the homogenizing elements (5) by the Rainbow solar cell and adjusting its distance to the focal plane of the curved mirror until the position of each sub-cell matches the corresponding spectral range.

C. External quantum efficiency

The EQE is a common and useful figure of merit in photovoltaics that quantifies the spectral contribution to the short circuit current density J_{sc} .⁵ Mathematically, the J_{sc} and EQE are related as follows:

$$J_{sc} = \int \frac{\phi(\lambda)}{E_{ph}(\lambda)} EQE(\lambda) q d\lambda. \quad (1)$$

Here, $\phi(\lambda)$ is the spectral irradiance (in units of energy/second/area), $E_{ph}(\lambda)$ is the photon energy, and q is the electron charge. By dividing $\phi(\lambda)$ by $E_{ph}(\lambda)$, we obtain the number of photo-generated electrons per unit time and area, which multiplied

by the charge of an electron and integrated over the entire spectrum, yields the current density J_{sc} . The standard *EQE* characterization involves the measurement of the photocurrent under narrowband monochromatic wavelength illumination, typically in short circuit conditions ($J_{sc,\lambda}$), for different central wavelengths in the range between 350 and 1100 nm.⁵ Narrowband illumination is typically obtained by spectrally filtering a broadband source, for example, using a monochromator. In that direction, the *EQE* can be calculated for each narrowband illumination condition as follows:

$$EQE(\lambda) = \frac{J_{sc,\lambda}/q}{P_{in}/E_{ph}(\lambda)}. \quad (2)$$

This corresponds to the ratio between the number of collected electrons and the number of incoming photons at a given wavelength. The narrower the light source, i.e., the more monochromatic it is, the better the resolution of the *EQE*. Note that this method to determine the *EQE* corresponds to the variant of steady-state, direct current (DC) mode without background illumination, which for organic solar cells yields reliable results.³⁴

In practice, the *EQE* is measured with SOLS employing the slit system, which comprises a set of complementary slit masks of 2 mm each centered at different wavelengths (see supplementary material, Fig. S3 and Fig. 7). In this way, SOLS transforms into a narrowband tunable light source. The power density of the spectrum resulting from each slit is measured with a thermopile, and the wavelength is given by the central wavelength of each slit spectrum. Figure 5 shows *EQE* measurements made with the slit system of SOLS compared to those attained with our custom-made *EQE* rig, which includes a broadband laser and a monochromator (purple curves). The results were obtained for OPVs with different bandgaps, for which the corresponding chemical structures as well as details about device structure and fabrication can be found in the supplementary material, Sec. S10 and Fig. S17. When light is collimated before

entering the Amici prism (orange data in Fig. 5), the SOLS *EQE* resolution is similar to that of the reference system in the spectral range between ~400 and 600 nm. For longer wavelengths, though, the wavelength resolution decreases drastically, resulting in a broadening effect of the *EQE*. This can be improved by enhancing the wavelength resolution, for example, by collimating and reducing the lateral width of the light entering the Amici prism (green data in Fig. 5). See Sec. IV and Fig. S6 of the supplementary material for further details on how to improve wavelength resolution in the long wavelength spectral range. Nevertheless, for our current implementation, the agreement between the SOLS *EQE* curves and those of the custom-made rig is excellent.

Interestingly, the *EQE* can also be extracted from a red or a blue sweep measurement performed in spectral splitting characterization mode (Fig. 6). In this characterization mode, we can consider that the difference between measurements for two consecutive dividing wavelengths λ_d is analogous to a narrowband measurement using a slit with a width equal to the spatial difference between the positions of the guillotine during the red or blue sweep. The measurement proceeds as follows: first, either a red or blue sweep is performed, and the J-V characteristics of the cell are recorded as a function of λ_d . From this set of data, one computes the solar cell parameters J_{sc} , open-circuit voltage V_{oc} , fill factor FF , and *PCE* vs λ_d , as shown in Fig. S16 of the supplementary material, for example. In analogy to a slit spectrum, $J_{sc,l}$ of Eq. (2) is computed by taking the difference of the J_{sc} obtained for two consecutive λ_d . The corresponding (pseudo-slit) power density P_{in} is then obtained from a previous calibration of the incident spectrum, which consists of separately measuring the spectrum and thus the power density at each λ_d and taking the difference for two consecutive ones. Hereafter, the *EQE* is computed using Eq. (2), as in the case of narrowband illumination. Notice that this procedure implies that *EQE* can be extracted from any Rainbow measurement at no additional cost other than for making the mentioned spectral calibration. Since this equipment-dependent calibration needs to be performed only once, this means that the

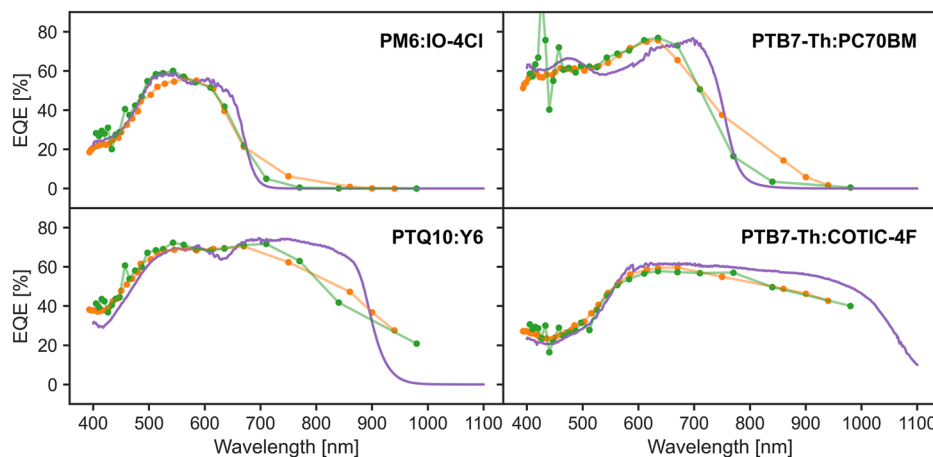


FIG. 5. Slit-EQE measurements with SOLS for collimated input light and collimated with lateral width reduction (orange and green data points joined by straight lines, respectively) compared with results obtained with a standard white laser coupled to a monochromator (purple curves). When SOLS input light is only collimated (orange curves), the results show comparable resolution between 400 and 600 nm, and it decreases drastically for higher wavelengths. In this range, the resolution improves when applying beam-width reduction at the entrance of the Amici prism (green curves).

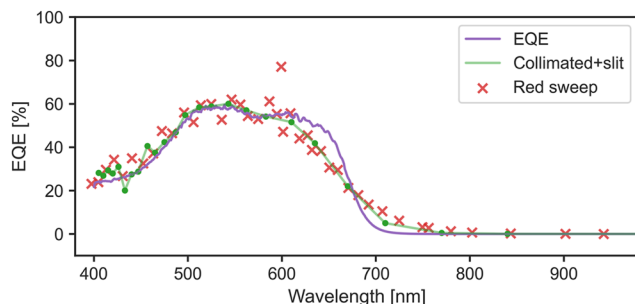


FIG. 6. EQE of a PM6:IO4-Cl cell (same cell as one in Fig. 5) calculated from a red sweep of a Rainbow measurement (red data points). The agreement with the reference EQE measured with a white laser and a monochromator (purple curve) is very good, as is the agreement with the slit-EQE measurement with SOLS with the collimated + slit resolution (green line).

SOLS setup also saves valuable measurement time. Details are given elsewhere.²¹

Notice that, as far as we know, this methodology of measuring EQE from a red (or a blue) sweep is a unique capability of the SOLS setup. As can be appreciated in Fig. 6, the agreement between the EQE obtained with the red sweep procedure and the more conventional monochromator-like mode with the slits system (when light is collimated and slit-reduced for higher spectral resolution) is excellent. The EQE could also be obtained from a blue-sweep measurement since the pseudo-slit resulting from both sweeps is exactly the same.

IV. SPECTRAL RESOLUTION AND OTHER SPECIFICATIONS

The main advantage of SOLS with respect to other light sources is its spectrum customization. This is strongly linked to the wavelength resolution and, therefore, to the wavelength distribution/separation along the plane where the filtering systems are placed. In order to be able to distinguish between two wavelengths, their intensity distributions in the plane need to be sufficiently separated in the lateral (wavelength) direction. This is directly related to the way the dispersive element, the double Amici prism, separates the light.^{31,32} For any refractive optical element, the separation between two adjacent wavelengths is determined by the difference in the deviation angles for the two wavelengths and the distance they travel. The former is governed by the wavelength variation of the refractive index (aka dispersion) of the two materials composing the double Amici prism. In the visible spectral range, and as a rule for any glass combination, this angle is higher for shorter wavelengths and, therefore, the wavelength resolution of the SOLS setup is higher in the blue as compared to the red part of the spectrum. The wavelength resolution or color separation can also be improved by increasing the distance between the prism and the mirror at the expense of increased equipment size.

There are, however, other factors that also impact the resolution, namely the degree of collimation (how paraxial the incident beam is) and the lateral extension (width) of the beam at the entrance of the double Amici prism. Ideally, if the input light is perfectly

collimated and enters the prism only in an infinitesimally thick vertical line, every photon with the same wavelength would have the same optical path through the prism, exiting at the same point and with the same angle. Therefore, one would expect a Dirac delta-like distribution of collimated light at the entrance of the double Amici prism to lead to a narrow Gaussian peak in the wavelength axis. A departure from this ideal situation occurs, for example, when light, though collimated, enters a finite thickness slit. The resulting distribution is expected to be a sum of various Gaussian functions corresponding to each infinitesimal slit comprising the finite slit width. Yet we have found that it is still more critical the effect of a poor collimation of the beam. For example, if one focused the beam with a cylindrical lens at the entrance of the Amici, there would be a distribution of incoming angles for photons with the same wavelength and, therefore, even if they entered the double Amici prism from exactly the same point, they would escape it with different angles. Therefore, one expects a broadening effect of the Gaussian distribution and a certain degree of color mixing. Both effects are detrimental for the spectral resolution and are mainly dependent on the input light beam: the thinner and more collimated it is, the better the color separation at the plane of the mask systems, thus improving the wavelength resolution.

The mentioned dependence on spectral resolution is best observed in the cascades of slit spectra shown in Fig. 7. The figure displays the spectra resulting from consecutive 2 mm slit masks when light enters the Amici prism in different ways. The left panel corresponds to the case when light is coming directly from the Xenon arc lamp. The middle panel is the case of previously collimated light, whereas the right panel represents the case of an incident beam which, apart from being collimated, is also reduced in width using a 2 mm wide slit at the entrance of the Amici prism. These data clearly show that measured spectra are much narrower when collimation and width-reduction are implemented at the entrance of the Amici prism, leading to a strong improvement in wavelength resolution for the same slit width (see also Fig. S6 of the supplementary material for the HWHM vs central wavelength relation, corresponding to the spectra shown in Fig. 7).

As usual, there is a trade-off between the spectral resolution and light throughput of the SOLS setup. It is clear that whatever the optics used for the collimation of a non-paraxial primary light source, there will be a certain penalty in light intensity, which is even higher when a slit is placed in front of the Amici prism. However, the best spectral resolution is not always necessary. The high spectral resolution is a requirement for the accurate measurement of the EQEs, whereas for the determination of the PCE, it is by far more important to achieve 1 sun power density and Class-A spectral matching.

Another important parameter of the setup is the *temporal stability*, which is expected to be mainly determined by the temporal stability of the input light source, i.e., the Xe-arc lamp in this case. The reason is that none of the SOLS components is moving or changing while a given spectrum is produced at the output of the equipment. To verify this hypothesis, however, we have measured the short term instability (STI) and long term instability (LTI) of both the light entering the SOLS apparatus as well as the light at its output. For this purpose, we have measured the time dependence of the light power with a silicon photodetector both at the entrance of the Amici prism and at the device-under-test location, i.e., positions

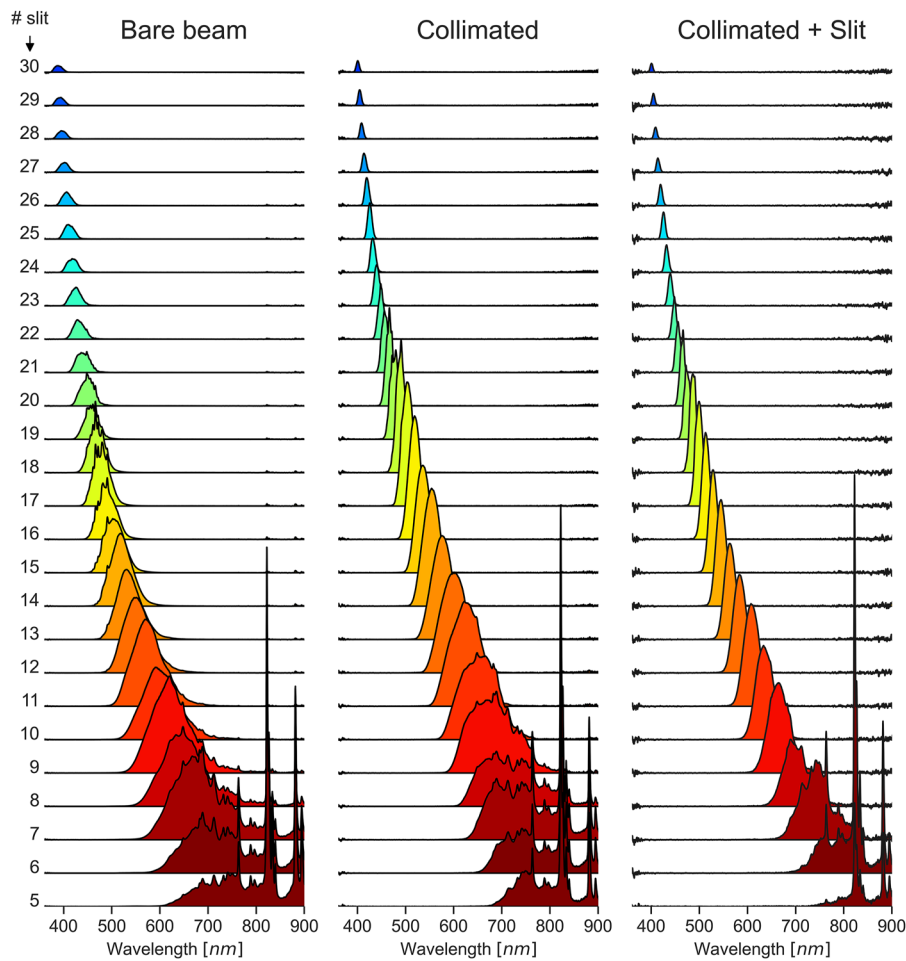


FIG. 7. Series of spectra shaped by SOLS corresponding to a set of slits of 2 mm width used for calibration of the system in the case of bare beam input light (left panel), collimated input light (middle panel), and collimated beam plus a laterally reduced width (right panel), entering the Amici prism. Collimated and collimated + slit data were multiplied by a factor of 4 and 10, respectively, with respect to the normal illumination data for the sake of clarity.

(3) and (6) in Fig. 1, respectively. The time instabilities are calculated according to

$$STI \text{ or } LTI(\%) = 100 \cdot \frac{P_{\max} - P_{\min}}{P_{\max} + P_{\min}}. \quad (3)$$

Here, P_{\min} and P_{\max} are the minimum and maximum recorded power over time. The time intervals are not well established, but depend on the solar simulator application. Here, we have considered the time elapsed during the measurement of the J-V curves, which in our case takes around 5 s. For the STI, power data were acquired every 10 ms for a total of 5 s, which represents the system stability during a J-V curve measurement. The process was repeated 5 times for statistics. Analogously, LTI data were acquired every 1 s for a total of 50 s, thus representing the power variation between different J-V curve measurements.

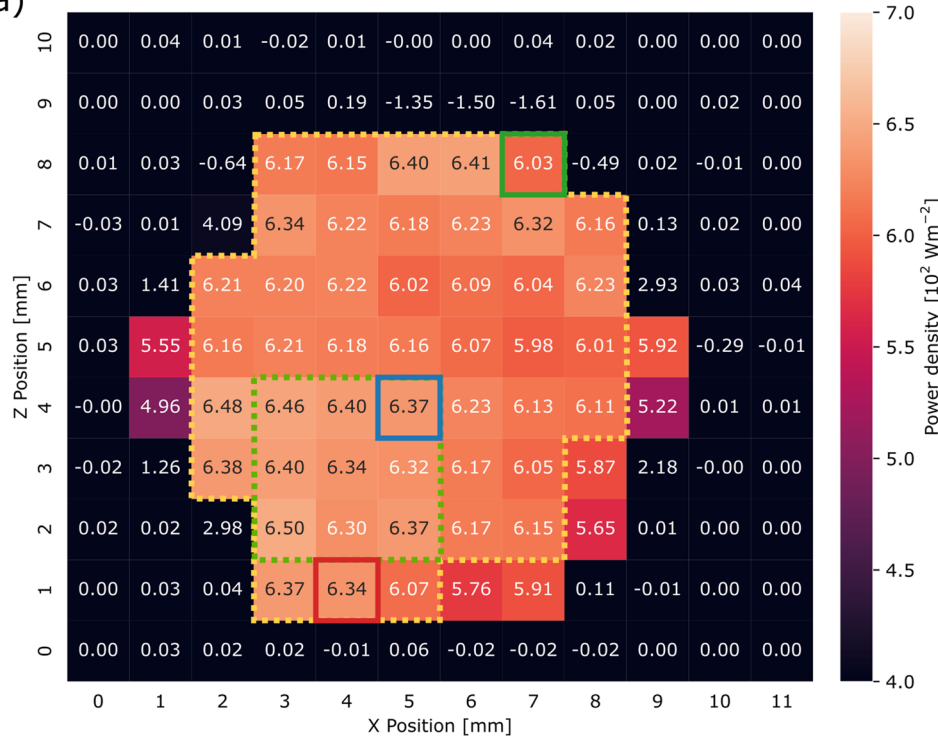
The results of the stability test are shown in Table I. In all cases, the light power instability over time is well below 1%, with the long-term instability being less than half of the short-term one. Moreover, the STI is statistically the same at both the input and the output. For the LTI, there is a difference, but it is not significant due to the small absolute value. In any case, these observations indicate that the SOLS setup does not cause any additional temporal instability compared to that of the xenon-arc lamp, the light source employed in this embodiment. The temporal stability is Class A according to ASTM standards since both STI and LTI are significantly lower than 2%.

Finally, we turn to the discussion of *spatial homogeneity* in areal-illumination mode concerning both light intensity and spectral shape. The light power density (in W/m^2) is then mapped out across the illuminated area at the device-under-test location, i.e., at the output facet of the homogenizing device consisting of a diffusing element in front of a homogenizing light pipe [(6) in Fig. 1]. The gadget used for the spot measurement of the light power

TABLE I. Short term instability (STI) and long term instability (LTI) of the light power at the entrance (input) and at the location of the device-under-test of the SOLS setup (output). Five measurements (J-V curves) were done for each situation, and the average and standard deviation are shown in the last row.

Measurement	STI (%)					LTI (%)				
	Input		Output			Input		Output		
1		0.73		0.88		0.30		0.22		
2		0.88		0.81		0.38		0.20		
3		0.69		0.62		0.28		0.27		
4		0.80		0.56		0.31		0.24		
5		0.78		0.88		0.39		0.21		
Average		0.78 ± 0.07		0.75 ± 0.15			0.33 ± 0.05		0.23 ± 0.03	

a)



b)

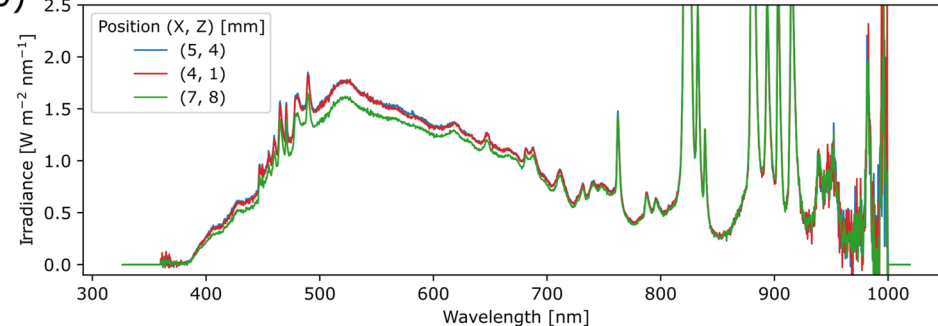


FIG. 8. (a) Spatial distribution of SOLS output light intensity in the plane of the light-pipe facet, where a grid of 11×10 pixels 2 was defined for spot measurements by scanning a small aperture (see text for details). The numbers inside the square pixels represent the measured light power density. The dashed yellow line encloses a large Class B region with 4.16% spatial non-uniformity, while the green dashed region has 1.56% spatial non-uniformity, corresponding to a Class A. (b) Spectra measured at three selected pixels marked on the grid with the corresponding colors (green, blue, and red solid line squares).

density consists of a small pinhole of $500\text{ }\mu\text{m}$ in diameter, mounted in front of the optical contraption that collects the light with an optical fiber for its spectral analysis with the Flame spectrometer (see Fig. S7 of the supplementary material). Using a motorized stage, the pinhole was moved over a grid of 11×10 pixels², with every pixel being $1 \times 1\text{ mm}^2$ in size, while recording the output light spectrum. In this way, we construct the pixelated power density map shown in Fig. 8(a). The illuminated hexagonal cross-section of the light pipe is easily recognizable as the bright area of the map. The number inside each square pixel represents the light power density obtained from the integrated intensity of the spectrum measured at each spot. The high homogeneity of the spatial distribution of the light intensity when SOLS is used in areal illumination mode is clearly apparent from the map in Fig. 8(a). In fact, the spatial inhomogeneity can be calculated in a similar way as the STI and LTI using Eq. (3). The intensity inhomogeneity measured across the area delimited by the yellow dashed line in Fig. 8(a), i.e., almost the entire light pipe facet, is 4.16%. This corresponds to a Class B spatial non-uniformity according to ASTM standards. Nevertheless, if we consider a smaller area like the one enclosed by the green dashed line, the non-uniformity reduces to 1.56%, making it Class A.

The same methodology was applied to test the spatial homogeneity of the output beam in terms of spectral shape, a particularly important specification for the SOLS setup. Figure 8(b) shows the spectra from three selected pixels, highlighted with solid lines of different colors on the grid in Fig. 8(a). Strikingly, the spectral shape appears to be totally independent of the position across the section of the output beam. This indicates that the (small) changes in the integrated power of Fig. 8(a) are mainly related to a change in the intensity of the spectrum rather than a change in its spectral shape. We point out that to attain such good spatial homogeneity in terms of spectral shape, the use of the diffuser in front of the light pipe is crucial (see supplementary material, Sec. S11, for the detrimental effects of removing the diffuser).

V. CONCLUSIONS AND OUTLOOK

In summary, we presented a novel spectral shaper illumination device with facile tunability that can be used to perform several standard photovoltaic tests (efficiency, EQE, intensity-dependent efficiency) with one piece of equipment, therefore, helping to accelerate material screening and enabling the discovery and optimization of novel multi-component materials for emergent PV technologies like organic PV, metal halide perovskites PV, all oxides PV, kesterites, etc. The same equipment can also be used as a light source for more advanced characterizations requiring intensity-dependent PV characterization, which is the case for the study of recombination processes in photovoltaics. The SOLS device also enables the development of many photovoltaic applications far from standard sunlight harvesting, including agrovoltas, indoor PV, building integrated PV (windows, sunshades, etc.), semitransparent PV, etc. SOLS is also able to measure the EQE of a solar cell in two different ways, the more standard way using the equipment as a tunable monochromator and a novel EQE measurement mode that emerges from the unique inherent spectral splitting characteristics of the setup.

One particularly attractive novel application of the SOLS light source is in the field of materials science for the development of multi-junction solar cells, both spectrally split as well as conventional tandem cells, aimed at highly efficient light-to-electricity conversion. To the best of our knowledge, there is no other light source capable of addressing the full characterization (multi-junction and single sub-cell characterization) of multi-junction solar cells. In view of the fact that tandem and spectrally split solar cells can increase power conversion efficiency up to two to three times more than that of single-junction cells,³⁵ this is a very promising implementation area of the SOLS system. Furthermore, the combination of intensity and spectral tailoring capabilities offered by SOLS leads to novel characterization methodologies that could help to better understand charge generation and loss mechanisms inside solar cells, especially in the case of OPV, where at least two materials (donor and acceptor) are involved in the dynamics of the charge-generation process.

In the future, we aim to further develop the unique spectral splitting capability of SOLS as well as improve several crucial specifications like the spectral resolution in the red-infrared and the automation of the spectral shaping unit. Regarding color separation, apart from the measures taken so far to improve spectral resolution, there is the possibility to replace the Amici prism with one of a more dispersive material such as F2 glass. This would require a radical change in setup geometry, though. For an automated spectral shaping/filtering module, we are considering several possibilities such as the implementation of a liquid-crystal display working in transmission or digital micro-mirror arrays. Finally, concerning the EQE measurements, we are also considering setting up the modulated variant using a light chopper hooked to a lock-in amplifier, including background illumination of the tested solar cell.

SUPPLEMENTARY MATERIAL

The supplementary material comprises additional information about the SOLS setup, a description of the mask calibration system, as well as the output spectrum assessment and its calibration, providing additional spectra as examples. It also includes a discussion about the dynamic range of the SOLS setup, the spectral splitting measuring mode, and details about the calibration of the spectral splitting dividing wavelength. Furthermore, information about different multi-junction device structures is provided, including the chemical structure of the organic materials and device geometry. Finally, the spatial homogeneity of the output beam is also considered.

ACKNOWLEDGMENTS

The Spanish Ministerio de Ciencia e Innovación (MICINN) is gratefully acknowledged for its support through Grant No. CEX2019-000917-S (FUNFUTURE) in the framework of the Spanish Severo Ochoa Center of Excellence program and the AEI/FEDER(UE) under Grant Nos. PID2021-128924OB-I00 (ISOSCELLES) and PDC2022-134001-I00 (SOLS-PV proof of concept). The authors also acknowledge the Catalan agency AGAUR for Grant No. 2021-SGR-00444. M.C.-V. acknowledges an FPI

fellowship (Grant No. PRE2019-089855) from MICINN cofinanced by the European Social Fund, and M.G.-R. acknowledges the scholarship Grant No. FPU16/02631 from the Spanish “Ministerio de Educación.” M.C.-V. and M.G.-R. also acknowledge the Ph.D. program in Materials Science from the Universitat Autònoma de Barcelona, in which both were enrolled.

AUTHOR DECLARATIONS

Conflict of Interest

The authors have no conflicts to disclose.

Author Contributions

Miquel Casademont-Viñas: Data curation (equal); Formal analysis (equal); Investigation (equal); Methodology (equal); Software (equal); Writing – original draft (equal). **Martí Gibert-Roca:** Data curation (equal); Formal analysis (equal); Investigation (equal); Methodology (equal); Software (equal); Writing – review & editing (equal). **Mariano Campoy-Quiles:** Conceptualization (equal); Formal analysis (equal); Funding acquisition (equal); Investigation (equal); Methodology (equal); Project administration (equal); Resources (equal); Supervision (equal); Writing – review & editing (equal). **Alejandro R. Goñi:** Conceptualization (equal); Formal analysis (equal); Funding acquisition (equal); Investigation (equal); Methodology (equal); Project administration (equal); Resources (equal); Supervision (equal); Writing – review & editing (lead).

DATA AVAILABILITY

All data generated or analyzed during this study are either included in this published article and its supplementary information file or are available from the corresponding author on reasonable request.

REFERENCES

- ¹World Energy Outlook 2022 – Analysis - IEA (n.d.).
- ²Renewable Energy Market Update - May 2022 – Analysis - IEA (n.d.).
- ³Solar PV Global Supply Chains – Analysis - IEA (n.d.).
- ⁴M. A. Green, E. D. Dunlop, G. Siefer, M. Yoshita, N. Kopidakis, K. Bothe, and X. Hao, “Solar cell efficiency tables (Version 61),” *Prog. Photovoltaics. Res. Appl.* **31**(1), 3–16 (2023).
- ⁵O. Almora, D. Baran, G. C. Bazan, C. Berger, C. I. Cabrera, K. R. Catchpole, S. Erten-Ela, F. Guo, J. Hauch, A. W. Y. Ho-Baillie, T. J. Jacobsson, R. A. J. Janssen, T. Kirchartz, N. Kopidakis, Y. Li, M. A. Loi, R. R. Lunt, X. Mathew, M. D. McGehee, J. Min, D. B. Mitzi, M. K. Nazeeruddin, J. Nelson, A. F. Nogueira, U. W. Paetzold, N. G. Park, B. P. Rand, U. Rau, H. J. Snaith, E. Unger, L. Vaillant-Roca, H. L. Yip, and C. J. Brabec, “Device performance of emerging photovoltaic materials (version 1),” *Adv. Energy Mater.* **11**(11), 2002774 (2021).
- ⁶S. K. Kurinec, *Emerging Photovoltaic Materials: Silicon and Beyond* (Scrivener Publishing LLC, 2018), p. 826.
- ⁷M. Grossberg, J. Krustok, C. J. Hages, D. M. Bishop, O. Gunawan, R. Scheer, S. M. Lyam, H. Hempel, S. Levcenco, and T. Unold, “The electrical and optical properties of kesterites,” *J. Phys. Energy* **1**(4), 044002 (2019).
- ⁸S. Parola, B. Julián-López, L. D. Carlos, C. Sanchez, S. Parola, B. Julián-López, L. D. Carlos, and C. Sanchez, “Optical properties of hybrid organic-inorganic materials and their applications,” *Adv. Funct. Mater.* **26**(36), 6506–6544 (2016).
- ⁹V. Adinolfi, W. Peng, G. Walters, O. M. Bakr, and E. H. Sargent, “The electrical and optical properties of organometal halide perovskites relevant to optoelectronic performance,” *Adv. Mater.* **30**(1), 1700764 (2018).
- ¹⁰J. Yan, X. Rodríguez-Martínez, D. Pearce, H. Douglas, D. Bili, M. Azzouzi, F. Eisner, A. Virbule, E. Rezasoltani, V. Belova, B. Döring, S. Few, A. A. Szumska, X. Hou, G. Zhang, H. L. Yip, M. Campoy-Quiles, and J. Nelson, “Identifying structure-absorption relationships and predicting absorption strength of non-fullerene acceptors for organic photovoltaics,” *Energy Environ. Sci.* **15**(7), 2958–2973 (2022).
- ¹¹Q. Wang and A. Abate, “Strategies toward stable perovskite solar cells,” *Adv. Mater. Interfaces* **5**(22), 1800264 (2018).
- ¹²A. Harillo-Baños, X. Rodríguez-Martínez, and M. Campoy-Quiles, “Efficient exploration of the composition space in ternary organic solar cells by combining high-throughput material libraries and hyperspectral imaging,” *Adv. Energy Mater.* **10**(1), 1902417 (2020).
- ¹³K. M. Yeom, S. U. Kim, M. Y. Woo, J. H. Noh, and S. H. Im, “Recent progress in metal halide perovskite-based tandem solar cells,” *Adv. Mater.* **32**(51), 2002228 (2020).
- ¹⁴D. CarloRasi and R. A. J. Janssen, “Advances in solution-processed multijunction organic solar cells,” *Adv. Mater.* **31**(10), 1806499 (2019).
- ¹⁵D. H. W. Li, N. T. C. Chau, and K. K. W. Wan, “Predicting daylight illuminance and solar irradiance on vertical surfaces based on classified standard skies,” *Energy* **53**, 252–258 (2013).
- ¹⁶M. Blumthaler, W. Ambach, and R. Ellinger, “Increase in solar UV radiation with altitude,” *J. Prog. Photovoltaics B: Biol.* **39**(2), 130–134 (1997).
- ¹⁷P. Faine, S. R. Kurtz, C. Riordan, and J. M. Olson, “The influence of spectral solar irradiance variations on the performance of selected single-junction and multijunction solar cells,” *Solar Cells* **31**(3), 259–278 (1991).
- ¹⁸J. A. Röhr, J. Lipton, J. Kong, S. A. Maclean, and A. D. Taylor, “Efficiency limits of underwater solar cells,” *Joule* **4**(4), 840–849 (2020).
- ¹⁹H. S. Ryu, S. Y. Park, T. H. Lee, J. Y. Kim, and H. Y. Woo, “Recent progress in indoor organic photovoltaics,” *Nanoscale* **12**(10), 5792–5804 (2020).
- ²⁰B. Minnaert and P. Veelaert, “A proposal for typical artificial light sources for the characterization of indoor photovoltaic applications,” *Energies* **7**(3), 1500–1516 (2014).
- ²¹M. R. Gibert-Roca, M. Casademont-Viñas, Q. Liu, K. Vandewal, A. R. Goñi, and M. Campoy-Quiles, “RAINBOW organic solar cells: Implementing spectral splitting in lateral multi-junction architectures,” *Adv. Mater.* (published online, 2023).
- ²²A. Mojiri, R. Taylor, E. Thomsen, and G. Rosengarten, “Spectral beam splitting for efficient conversion of solar energy—A review,” *Renewable Sustainable Energy Rev.* **28**, 654–663 (2013).
- ²³V. Esen, S. Sağlam, and B. Oral, “Light sources of solar simulators for photovoltaic devices: A review,” *Renewable Sustainable Energy Rev.* **77**, 1240–1250 (2017).
- ²⁴J. Vollbrecht, V. V. Brus, S. J. Ko, J. Lee, A. Karki, D. X. Cao, K. Cho, G. C. Bazan, and T. Q. Nguyen, “Quantifying the nongeminate recombination dynamics in nonfullerene bulk heterojunction organic solar cells,” *Adv. Energy Mater.* **9**(32), 1901438 (2019).
- ²⁵D. Lübke, P. Hartnagel, M. Hülsbeck, and T. Kirchartz, “Understanding the thickness and light-intensity dependent performance of green-solvent processed organic solar cells,” *ACS Mater. Au* **3**, 215–230 (2023).
- ²⁶P. Hartnagel and T. Kirchartz, “Understanding the light-intensity dependence of the short-circuit current of organic solar cells,” *Adv. Theory Simul.* **3**(10), 2000116 (2020).
- ²⁷D. Glowienka, Y. Galagan, D. Glowienka, and Y. Galagan, “Light intensity analysis of photovoltaic parameters for perovskite solar cells,” *Adv. Mater.* **34**(2), 2105920 (2022).
- ²⁸F. C. Krebs, K. O. Sylvester-Hvid, and M. Jørgensen, “A self-calibrating led-based solar test platform,” *Prog. Photovoltaics. Res. Appl.* **19**(1), 97–112 (2011).

- ²⁹E. López-Fraguas, J. M. Sánchez-Peña, and R. Vergaz, “A low-cost LED-based solar simulator,” *IEEE Trans. Instrum. Meas.* **68**(12), 4913–4923 (2019).
- ³⁰A. V. Hill, M. Amnon, and O. Bachar, U.S. patent 10422508B2, issued on 2019-09-24. (<https://patents.google.com/patent/US10422508B2/en?oq=US10422508>).
- ³¹G. B. Donati, “Intorno alle strie degli spettri stellari,” *Il Nuovo Cimento (1855-1868)* **15**, 292–304 (1862).
- ³²N. Hagen and T. S. Tkaczyk, “Compound prism design principles, I,” *Appl. Opt.* **50**(25), 4998–5011 (2011).
- ³³G. Burwell, O. J. Sandberg, W. Li, P. Meredith, M. Carnie, and A. Armin, “Scaling considerations for organic photovoltaics for indoor applications,” *Sol. RRL* **6**(7), 2200315 (2022).
- ³⁴S. Ravishankar, C. Aranda, P. P. Boix, J. A. Anta, J. Bisquert, and G. García-Belmonte, “Effects of frequency dependence of the external quantum efficiency of perovskite solar cells,” *J. Phys. Chem. Lett.* **9**(11), 3099–3104 (2018).
- ³⁵M. A. Green and S. P. Bremner, “Energy conversion approaches and materials for high-efficiency photovoltaics,” *Nat. Mater.* **16**(1), 23–34 (2016).